Contact-line instability caused by air rim formation under non-splashing droplets

Min Pack[1], Paul Kaneelil[1], Hyoungsoo Kim[2,3], and Ying Sun[1,*]

[1]*Department of Mechanical Engineering and Mechanics, Drexel University, Philadelphia, PA, USA*
[2]*Department of Mechanical and Aerospace Engineering, Princeton University, Princeton, NJ, USA*
[3]*Department of Mechanical Engineering, KAIST, Daejeon, South Korea*

ABSTRACT. Drop impact is fundamental to various natural and industrial processes such as rain-induced soil erosion and spray coating technologies. The recent discovery of the role of the air entrainment between the droplet and impacting surface has produced numerous works uncovering the unique physics that correlates the air film dynamics to the drop impact outcomes. In this study, we focus on the post-failure air entrainment dynamics for We numbers well below the splash threshold under different ambient pressures and elucidate the interfacial instabilities formed by air entrainment at the wetting front of impacting droplets on perfectly smooth, viscous films of constant thickness. A high-speed total internal reflection microscopy technique accounting for the Fresnel reflection at the drop-air interface allows for *in situ* measurements of an entrained air rim at the wetting front. The presence of an air rim is found to be a prerequisite to the interfacial instability which is formed when the capillary pressure in the vicinity of the contact line can no longer balance the increasing gas pressure near the wetting front. A critical capillary number for the air rim formation is experimentally identified above which the wetting front becomes unstable where this critical capillary number inversely scales with the ambient pressure. The contact line instabilities at relatively low We numbers (We ~ O(10)) observed in this study provide insight into the conventional understanding of hydrodynamic instabilities under drop impact which usually require We >> 10.

[*]Corresponding author. Tel.:+1-215-895-1373; fax: +1-215-895-1478; Email: ysun@coe.drexel.edu.

Introduction

The omnipresence of drop impact in both natural and industrial processes has led to an abundance of studies in various conditions and configurations[1-3]. From rain-fall induced aerosol release[4] to the development of self-cleaning lubricant-infused surfaces (LIS)[5-7], droplet-surface interactions continue to intrigue the scientific community. The technological implications of drop impact studies are legion: inkjet printing[8], combustion[9], spray coating[10-11] and cooling technologies[12], as well as agricultural applications[13-17], are all dependent on droplet-surface interactions. Recent studies in drop impact dynamics have probed the physics of droplet bouncing[18] and splashing[19] using high speed imaging. In the former, an entraining air film allows the droplet to "skate" on top of an air film on the order of O(100 nm)[18, 20]. In the latter, at a high Weber number ($\mathrm{We} = \rho_l U_0^2 R_0 / \sigma_l$), the drop impact destabilizes the droplet contact line due to the compressibility of the air where ρ_l is the density of the liquid droplet, U_0 the impact velocity, R_0 the droplet radius, and σ_l the surface tension of the liquid droplet[19].

While asperities on solid surfaces cause stochastic failure of the interstitial air film[18, 21-23], on atomically smooth, lubricated substrates with a thin oil film, a recent study has shown that the failure of the air layer is predictable[24]. Prior to a direct drop-film contact, an interstitial air layer is found to deform the droplet bottom and forms a central air bubble known as the "dimple" as well as a "kink" located at the first inflection point away from the dimple[25]. For an intermediate Weber number, $2 < \mathrm{We} < 10$, the air film fails due to the drop top surface crashing down resulting from the impact-induced capillary waves at the drop bottom surface and creating an inverted drop-air interface that pierces the air film at the dimple[24]. Further increasing the Weber number (i.e., $\mathrm{We} > 10$) shifts the failure mechanism to a disjoining pressure dominant regime where the air film consistently fails at the kink.

Once the air film fails and the droplet wets the impacting surface (i.e., the thin oil film), the subsequent contact line instability at the wetting front is poorly understood although it has been probed by many studies to date[26-30]. For instance, Li et al.[31] has observed an unstable contact line for drop impact on a highly viscous oil film but has concluded that the cause of the instability was unclear, likely due to the limitation of the measurement techniques. In drop splashing studies, several instability mechanisms have been proposed for an unstable contact line under drop impact, including the Rayleigh-Taylor (RT)[32-34] and Kelvin-Helmholtz (KH)[35-36] instabilities. Both RT and KH instabilities at the drop-air interfaces require large We to splash, typically on the order of We ~ O(10^2). For instance, the KH instability was investigated by varying the ambient air pressure, P_0, between 0.01 to 1 atm and drop splashing was found suppressed at $P_0 \leq 0.3$ atm as a result of the reduced drop-air velocity jump[19, 35-36].

Another relevant wetting instability has been identified in coating flows[37-38] for when a moving substrate is coated with a liquid at a high velocity such that the advancing liquid phase cannot successfully displace the receding gaseous phase near the contact line[39-43]. Vandre et al.[39] has shown that, above a critical capillary number $\mathrm{Ca} \sim \mu_l V_0 / \sigma_l$, where V_0 is the contact line velocity, μ_l is the dynamic viscosity of the droplet, and σ_l the surface tension of the droplet, the coating front transitions from two-dimensional to three-dimensional as the air pressure increases near the contact line and eventually entrains a rim of air. Sprittles[41] studied the effect of a slip condition in coating flows which becomes important when the thickness of the air film next to the wetting front reaches the mean free path of the ambient air O(100 nm). Li et al.[44] has also probed the importance of the rarefied gas effects experimentally and has found multiple contact points upon which wetting begins.

In this work, we focus on the post air film rupture dynamics and study the instabilities of the contact line of a droplet impacting on a flat thin oil film well below the splash thresholds under different ambient pressures. We differentiate our work from the splashing studies that focus on We >> 10[10,19,23,29,33-36,54] by highlighting the importance of the capillary pressure near the wetting front as compared with the gas pressure. The impacting surface is an atomically smooth surface which thus allows the air film underneath the drop to fully develop and to influence the wetting dynamics as the droplet pushes against the air film. We directly measure the instantaneous air film morphology and post-rupture drop-film wetting dynamics via total internal reflection microscopy (TIRM) inside a custom-built vacuum chamber. An air "rim" is detected at the wetting front above a critical capillary number Ca_c, where the Ca_c scales inversely with the chamber pressure, P_0 (i.e., $Ca_c \sim 1/P_0$). The formation of this air rim is found to be the prerequisite of the finger-like contact line instability at We ~ O(10) and is suppressed at low ambient pressures.

Experimental Methods

In this study, two high-speed cameras were used to simultaneously capture the drop impact dynamics in a custom-built vacuum chamber from the bottom at 2.7 μm/pixel recording at 25,000 frames per second (fps) (Phantom, V711) and from the side at 22.5 μm/pixel recording at 5,000 fps (Edgertronic), as depicted in Figure 1a. The total internal reflection microscopy (TIRM) from the bottom view camera was used to directly measure the air film profile near the droplet wetting front. The TIRM setup utilizes the evanescent wave generated by light totally reflected at an interface to probe the location of another interface[45]. A right-angled prism (PS913, ThorLabs) was used to provide an incident angle of θ_1 = 49.9° on the oil-air interface, which is greater than the critical angle for total internal reflection on the oil-air interface but less than the critical angle for

total internal reflection of the oil-droplet interface. Therefore, once the droplet makes contact with the oil film, light is refracted into the droplet and totally frustrates the evanescent wave registering as black spots in the camera and white when the air film thickness *h* is greater than the wavelength of the light. The detectable air film thickness of the TIRM setup lies between the maximum value approximated by the wavelength of the light source, λ (e.g., M660 with $\lambda \approx 665$ nm, ThorLabs) and the minimum thickness limited by the linearity of the camera sensor where the sensitivity is nonlinear close to the lowest grayscale values of the images (e.g., completely black corresponding to $h \approx 0$ - 20 nm)[46]. If all of the energy of the evanescent wave presumably passes into the third medium (e.g., the evanescent wave is totally frustrated by the droplet), the air film thickness, *h*, is then calculated by $h = -\beta \log(1 - I(r,z,t)/I(r,z,0))$, where β is the decay length of the evanescent wave and $I(r,z,t)$ is the local grayscale intensity normalized by the initial grayscale intensity $I(r,z,0)$[18, 47-48]. A recent work by Shirota et al.[46] reported the importance of the reflected components of the frustrated evanescent wave. Such that the assumption of total energy transfer into the third medium is incomplete, which means that the incident light always has transmitted and reflected components described by the Fresnel equations to be dependent on the polarization of the light (e.g., p-polarized light used in this study). The total reflected component, $\hat{r}$, is related to the refractive indices where the oil film, air and droplet denoted by n_1, n_2, and n_3, respectively, as well as the incident angles at each interface given by θ_1, θ_2 and θ_3, respectively, following Shirota et al.'s[46] description as

$$\hat{r} = \frac{\left(\frac{n_2\cos\theta_1 - n_1\cos\theta_2}{n_2\cos\theta_1 + n_1\cos\theta_2}\right) + \left(\frac{n_3\cos\theta_2 - n_2\cos\theta_3}{n_2\cos\theta_3 + n_3\cos\theta_2}\right)\exp\left(j\left(\frac{4\pi h}{\lambda}\sqrt{n_2^2 - n_1^2\sin^2\theta_i}\right)\right)}{1 + \left(\frac{n_2\cos\theta_1 - n_1\cos\theta_2}{n_2\cos\theta_1 + n_1\cos\theta_2}\right)\left(\frac{n_3\cos\theta_2 - n_2\cos\theta_3}{n_2\cos\theta_3 + n_3\cos\theta_2}\right)\exp\left(j\left(\frac{4\pi h}{\lambda}\sqrt{n_2^2 - n_1^2\sin^2\theta_i}\right)\right)}, \quad (1)$$

where j is an imaginary unit. Using Eq. (1), the air film thickness may be plotted against $|\hat{r}|^2$. Based on the h to $|\hat{r}|^2$ correspondence, each experimentally measured value of the normalized reflection intensity $|\hat{r}|^2 \equiv I(r,z,t)/I(r,z,0))$ directly determines the local air film thickness, h. We calibrated our TIRM measurements against Shirota et al.'s corrections and results from the reflection interference microscopy (RIM) with good agreements as shown in Figure 1b. In this study, we utilized the TIRM technique that enables the measurement of the air film thickness less than ≈100 nm in the vicinity of the contact line, while the RIM is only capable of capturing the air film thickness greater than 100 nm.

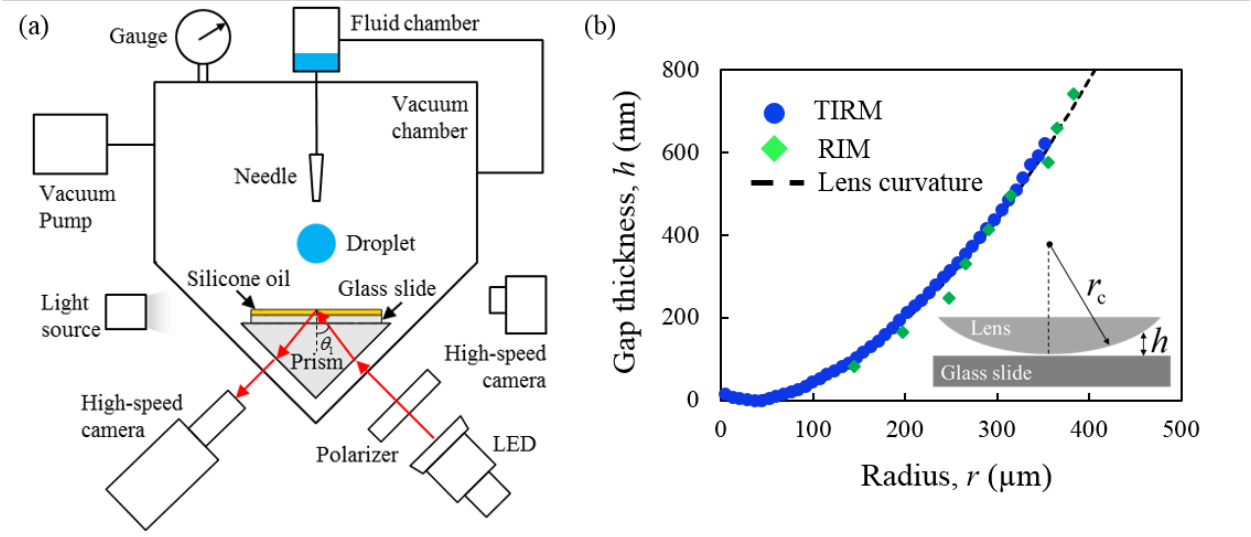

Figure 1. (a) Schematic of the experimental setup where a total internal reflection microscopy (TIRM) setup is housed in a vacuum chamber. (b) The TIRM calibration with the reflection interference microscopy technique for a lens with a known radius of curvature (r_c = 103 mm).

Aqueous droplets of glycerine and isopropanol (IPA) mixture with varying viscosities of 10.7 – 99.7 mPa·s impinged on a silicone oil film of 970 mPa·s (Sigma Aldrich) and thickness ≈ 2.7 μm coated on a glass slide (#1 float glass, Chemglass). The thickness of the oil film was accurately

obtained using a spin coater (Laurell) with the use of a known surface area and the weight of the film, tested over 30 measurements. The thin film thickness by the spin coating method was then confirmed via reflectometry (Filmetric F-20). The viscous oil film has a perfectly smooth surface[24] where the surface deformation is negligible, although such deformation may become important for thicker oil films as in soft solid substrates[49]. For the impinging droplet, the surface tension between the liquid droplet and air was controlled by mixing with IPA (e.g., 6% IPA for 40 mN/m and 12% IPA for 33 mN/m). Since the droplet is immiscible to the oil film below, there exist a triple line among the air, droplet and oil film and an associated droplet-oil surface tension[33]. The ambient pressure was controlled inside of a custom-built vacuum chamber between 0.18 – 1.00 atm. The radius of the droplet, a_0, was about 0.90 mm and the drop was dispensed through a hypodermic needle. The viscosity of the droplets was measured using a Brookfield DV+II Pro viscometer and the surface tension was measured using an Attension Sigma 701 tensiometer. Table 1 shows the list of the parameters used throughout this study.

Table 1. The list of the experimental conditions. Here μ_l is the viscosity, ρ_l the density, σ_l the surface tension between the droplet and air, a_0 the droplet radius, and U_0 the impact velocity of the drop, and P_0 is the chamber pressure.

	Droplet: Glycerine-IPA-Water (wt%)					Oil Film $\delta_{oil} \approx 2.7$ μm
	60-0-40	60-6-34	60-12-28	80-0-20	85-0-15	
μ_l [mPa s]	10.7	13.9	16.7	54.5	99.7	970
ρ_l [kg/m^3]	1141	1119	1098	1198	1213	970
σ_l [mN/m]	69.7	40.0	33.0	68.2	67.9	21.2
a_0 [mm]	0.904 ± 0.052					
U_0 [m/s]	0.9 – 1.4					
P_0 [atm]	0.18 – 1.00	1.00				

Results

Observation of a contact line instability

Figure 2a shows the bottom-view TIRM images of a drop (We ≈ 13 and $\mu_l \approx 10.7\ \mathrm{mPa \cdot s}$) wetting on a silicone oil film of 2.7 μm thickness and viscosity of $970\ \mathrm{mPa \cdot s}$. Once the droplet contacts the thin oil film, the wetting front between the drop and oil layer first traps an air rim delineated by a jump in the brightness of the periphery of the contact line to form periodic fingers from the onset of wetting around $t/t_f \approx 0.16$, where t_f denotes the time when the fingers finally disappear and $t_f \approx 0.72$ ms for the condition considered here. Between the time interval of $t/t_f \approx$ 0.16 – 0.66, both the amplitude and the wavelength of the fingers continue to grow as the droplet spreads radially as clearly observed in Figure 2a. Up through $t/t_f \approx 0.66$, the wetting front displays a characteristic "air film" as indicated by the grayscale intensity, the thickness of the air film is limited by the optics of the TIRM setup where the thickness range of 20 nm $\lesssim h \lesssim$ 600 nm sets the inner and outer radial bounds of the air film in each TIRM image. Here, $t = 0$ is the instant

when the droplet comes into the field of view of the TIRM setup at the air film thickness $h \approx$ O(100 nm) [18, 47, 50]. Note that the air film thickness resolution is in the single nanometer scale using the TIRM setup[18]. Notably, while the bottom-view TIRM images (Figure 2a) display a finger-like instability, it is undetectable from the side-view images in Figure 2b given that the finger-like structures are very small and are hidden due to backlighting.

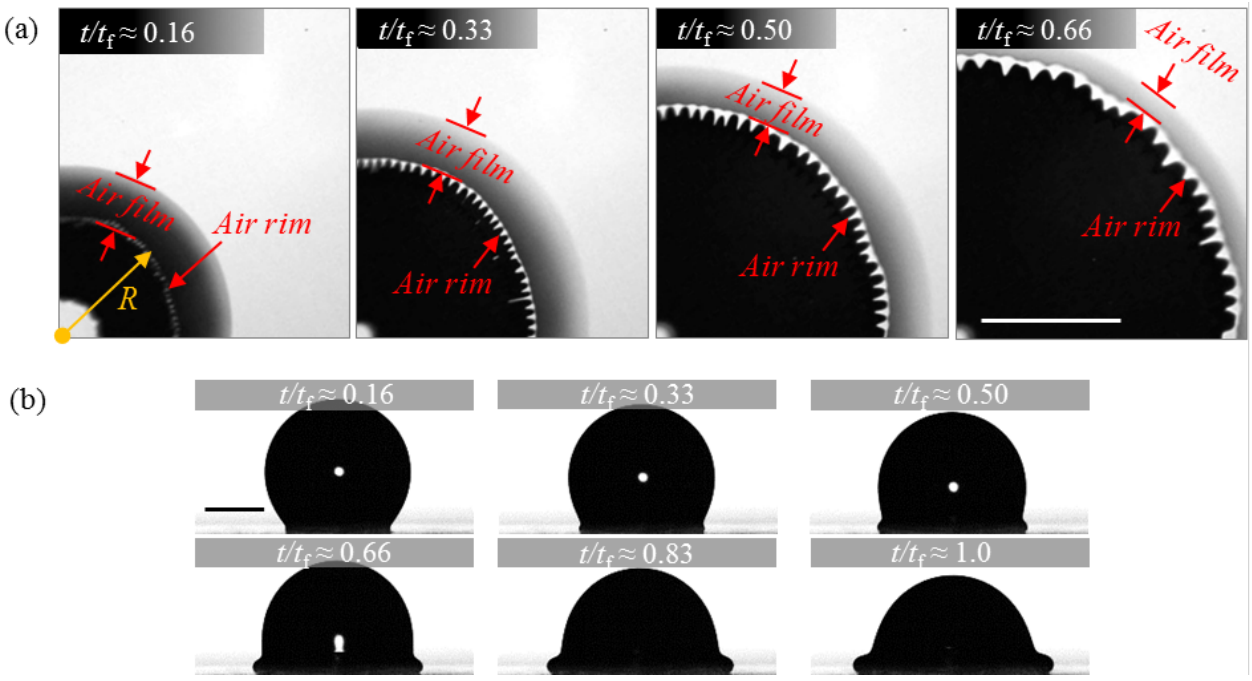

Figure 2. (a) Image sequence of a drop of We ≈ 13 and $\mu_l \approx 10.7\,\text{mPa}\cdot\text{s}$ impacting on a silicone oil film of 2.7 μm thickness and viscosity of 970 mPa·s at 1 atm obtained using total internal reflection microscopy. The time t is normalized by the time for the fingers to finally disappear as represented by t_f where the scale bar represents 0.5 mm. (b) Corresponding side-view image sequence where the scale bar represents 1 mm.

When the ambient air pressure is decreased from 1 atm to 0.8 atm while keeping other parameters the same, the air rim appears by $t/t_f \approx 0.16$, grows through $t/t_f \approx 0.33$ and then the wetting front becomes undulated by $t/t_f \approx 0.66$ with $t_f \approx 0.72$ ms as shown in Figure 3. A time

delay in the formation of the fingers in Figure 3 is observed compared to the 1 atm case. We presume this delay is due to a decrease of the air density caused by the lower ambient pressure (0.8 atm)[41] and thus for a similar contact line instability at the wetting front it takes more time to build up the air compared to the 1 atm case. Similar to Figure 2, $t/t_f \approx 1$ represents the instant in time when the fingers disappear, which is measured using the TIRM technique.

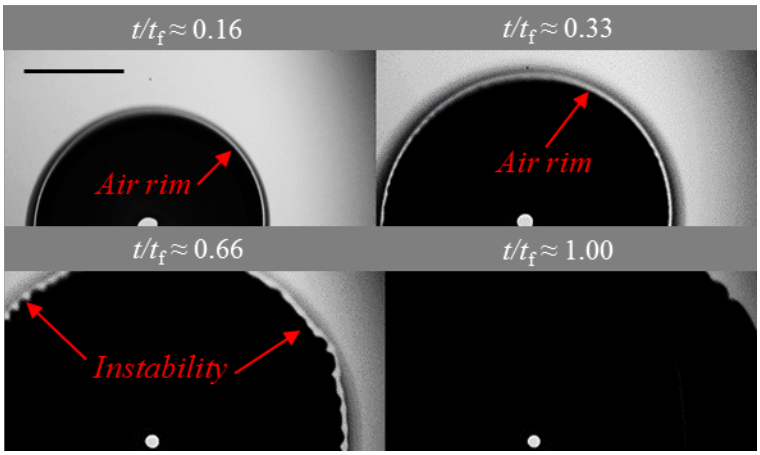

Figure 3. Image sequence of a drop of We ≈ 13 and $\mu_l \approx 10.7$ mPa·s impacting on a silicone oil film of 2.7 µm thickness and viscosity of 970 mPa·s at the chamber pressure of 0.8 atm, which is obtained using total internal reflection microscopy. The scale bar represents 0.5 mm.

To examine the effect of the droplet viscosity, we performed drop impact tests by varying the droplet viscosity (μ_l) between 10.7 mPa·s to 99.7 mPa·s. Figure 4a shows the evolution of three-dimensional shape of the air rim entrainment for a droplet viscosity of $\mu_l \approx 10.7$ mPa·s on the 2.7 µm thick silicone oil layer corresponding to the image sequence in Figure 2a. From $t \approx$ 0.12 ms to 0.24 ms, the air rim propagates radially outward, which is clearly observed by TIRM where by $t \approx$ 0.24 ms, the air rim growth is axisymmetric. An air pocket, known as the dimple, is captured at the center of the droplet, which has been well characterized in the past[21-22, 51-54]. At t

≈ 0.72 ms (see Figure 4a) the instability is suppressed where there are no more fingers or air rim near the contact line. Increasing the viscosity of the droplet by a factor of 10 (i.e., $\mu_l \approx 99.7$ mPa·s) as shown in Figure 4b, at the contact line, the higher viscosity droplet has a slower initiation and termination in the air rim. The rate of droplet spreading radially outward is stunted by the higher resistance to flow which reduces the rate at which the air underneath the droplet is displaced. Therefore, the air velocity in the air rim is reduced leading up to the delay in the air pressure buildup[39]. For example, an air rim has formed at $t \approx 0.12$ ms for the low viscosity case but not until at $t \approx 0.36$ ms for the high viscosity case. Similarly, the air rim is suppressed by $t_f \approx 0.72$ ms for $\mu_l \approx 10.7$ mPa·s whereas $t_f \approx 1.8$ ms for $\mu_l \approx 99.7$ mPa·s. By $t \approx 0.60$ ms for $\mu_l \approx 99.7$ mPa·s (see Figure 4b), the air rim is pronounced and continues to grow axisymmetrically with increasing the air rim height until it reaches the maximum TIRM resolution of $h_{max} \approx 600$ nm by $t \approx 0.80$ ms.

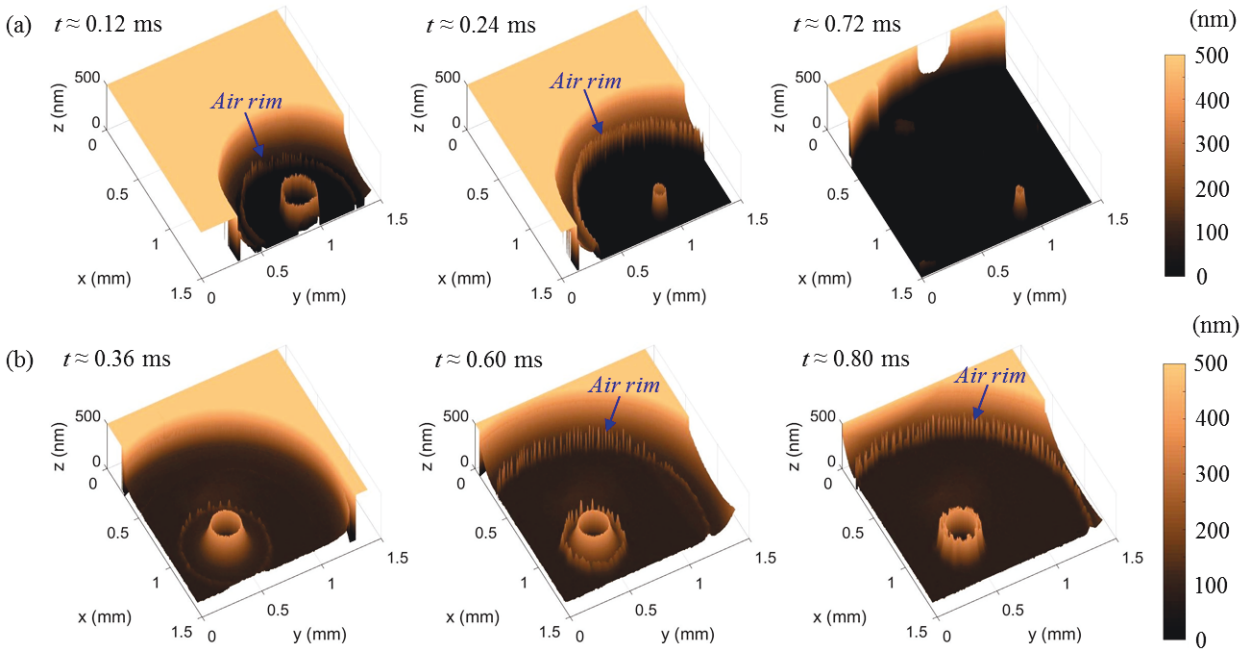

Figure 4. Reconstructed three-dimensional post-failure air film profiles from total internal reflection microscopy depending on the droplet viscosity (a) $\mu_l \approx 10.7$ mPa·s and (b) $\mu_l \approx 99.7$ mPa·s both at We ≈ 13 on a silicone oil film of 2.7 µm thickness and viscosity of 970 mPa·s at 1 atm.

As shown in Figure 5a, utilizing the TIRM technique, the evolution of the air film morphology next to the propagating wetting front is analyzed directly between two propagating fingers to obtain a cross-section of the air rim from the grayscale images for We ≈ 13 and $\mu_l \approx 99.7$ mPa·s corresponding to the case shown in Figure 4b. Figure 5a presents that the evolution of the air film thickness as the droplet spreads where the gray dashed line represents the air film morphology prior to the air rim formation and $t_f \approx 1.8$ ms for the conditions considered here.

Now we evaluate the importance of different pressure contributions prior to and during air rim formation as the drop spreads radially outward. For the air entrainment in coating applications

such as a solid plate plunging into a liquid bath, the two-dimensional wetting front turns three-dimensional when the capillary pressure, P_l, at the wetting front is balanced with the gas pressure, P_g (e.g., $P_g \sim P_l$) [39]. The liquid-gas interface is deformed due to the continuous buildup of the gas pressure near the contact line while the critical pressure balance of $P_g \sim P_l$ holds at the inflection point of the liquid-gas interface. Similarly, in drop wetting conditions, an inflection point in the drop-air interface at a distance *w* from the contact line forms as a result of the air pressure buildup next to the moving contact line as shown in the top frame of Figure 5b. As the air continues to accumulate near the contact line, an air rim is formed between the contact line and the inflection point of the drop-air interface as shown in the bottom frame in Figure 5b. Hence, in our study, the instant prior to the air rim formation is shown by the gray dashed line in Figure 5b, where *w* is the horizontal distance between the contact line and the inflection point. The curvature κ of the inflection point prior to the rim formation is approximated as $\kappa \sim 1/w$ where $w \sim \mathrm{O}(10^{-6})\,\mathrm{m}$ which is on the order of the lateral resolution of the camera at ≈ 2.7 μm such that $P_l \sim \sigma_l \kappa$ and $P_l \sim \mathrm{O}(10^4)\,\mathrm{Pa}$ assuming $\sigma_l \sim O(10^{-2})\,\mathrm{N/m}$. As the wetting front entrains more air in the rim, the *w* also grows between $w \sim \mathrm{O}(10^{-6} - 10^{-5})$ during drop spreading. For the largest value of *w* during spreading (e.g., $w \approx 50$ μm), the capillary pressure decreases to $P_l \sim \mathrm{O}(10^3)\,\mathrm{Pa}$. The inertial pressure is scaled as $P_i \sim \rho_l U_0^2 \sim \mathrm{O}(10^3)\,\mathrm{Pa}$ and thus we neglect the inertial pressure which is an order of magnitude smaller than the capillary pressure at early times when $P_l \sim \mathrm{O}(10^4)\,\mathrm{Pa}$. Since the ratio of the air film thickness to the drop radius, $h_{\min}/a_0 << 1$, applying the lubrication approximation to the axisymmetric air film, it follows $\partial P_g/\partial r \approx \mu_g \partial^2 u_r/\partial z^2$. The gas pressure at the inflection point hence scales as $P_g \sim \mu_g V w/h_{\min}^2$, where $h_{\min} \sim \mathrm{O}(10^{-8})\,\mathrm{m}$, $\mu_g \sim \mathrm{O}(10^{-5})\,\mathrm{Pa{\cdot}s}$

and the instantaneous wetting velocity, V, which varies between 1 to 0.7 m/s over the course of $t/t_f \approx 0.20$ and $t/t_f \approx 0.48$. We utilize the initial wetting velocity V_0, which is on the order of 1 m/s throughout the study. During the wetting process, the gas pressure first increases due to the air buildup near the contact line to form an air rim at sometime between $t/t_f \approx 0.20$ and $t/t_f \approx 0.28$ when $P_g \sim P_l$ at the inflection point. We also note that the microscopic contact angle[55] measured by the TIRM method during this period is large (≈180°) considering that the air film thickness is on the order of 10 nm whereas the radial length scale is on the order of 1 mm. The gas pressure then decreases between $P_g \sim O(10^6)$ Pa at $t/t_f \approx 0.28$ to $P_g \sim O(10^5)$ Pa at $t/t_f \approx 0.44$ during which the height of the air rim grows rapidly entraining more air to the rim as shown in Figure 5a. As the gas pressure continues to decrease, it reduces faster than the capillary pressure and finally becomes smaller than the capillary pressure causing the air rim and fingers to disappear. This is evidenced for a lower viscosity case in the last frame of Figure 4a, where the instability is suppressed at $t \approx 0.72$ ms. Consequently, three regimes are identified as the contact line advances: in the first regime, air pressure builds up and air rim forms; in the second regime, air rim grows and the amplitude of fingers increases; and finally, the air rim disappears and the fingers are suppressed.

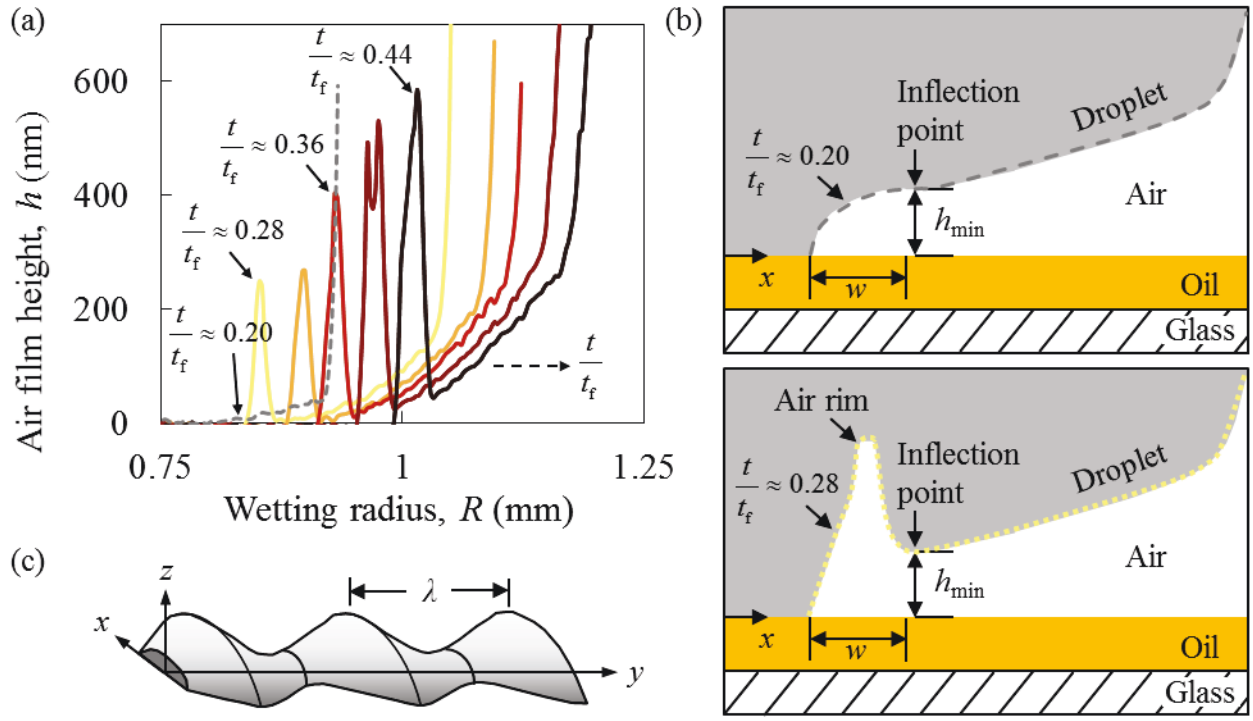

Figure 5. The air rim formation and propagation on an oil film surface while the droplet impacts. (a) Direct measurement of the air rim formation for We ≈ 13 and $\mu_l \approx 99.7\,\mathrm{mPa\cdot s}$ on the silicone oil film of 2.7 μm thickness and viscosity of 970 $\mathrm{mPa\cdot s}$ at 1 atm. The dashed gray line represents $t/t_f \approx 0.20$ where $t_f \approx 1.8$ ms and the colored lines represents the air film profiles ($\Delta t/t_f$=0.04) with the air rim formation as well as the evolution of the instability. The dashed black arrow represents the direction of propagation of the wetting front. (b) A schematic of the formation of the air rim with the gray dashed line representative of the air profile prior to the air rim formation ($t/t_f \approx 0.20$) and with the yellow dotted line representative of the liquid-air interface profile after air rim formation ($t/t_f \approx 0.28$). The figure is not to scale. (c) A schematic of the three-dimensional perturbed air rim shape with a characteristic wavelength, λ.

Critical capillary number for air rim formation

In order to understand the condition under which the air rim forms, a model is considered for the pressure balance at the drop-air interface next to the wetting front. The model assumes that the air film is formed between the droplet and the impacting surface below, which is modeled by the lubrication approximation given the large aspect ratio of the air film thickness h ~ O(100 nm)

compared to the radial length scale R ~ O(1 mm). We also probe the significance of the slip effects at the liquid-gas interface given by the Knudsen number, Kn, which is defined as $\mathrm{Kn} = l/L$. Here, l is the mean free path of air and L the characteristic length scale of the air film defined as $h_{\min,0}$, the height of the inflection point when the air film fails under atmospheric pressure (e.g., $h_{\min,0}$ ~ O(10)nm). Presuming that the gas molecules are rigid spheres, $l = k_{\mathrm{B}}T/(\sqrt{2}\pi P_0 l_{\mathrm{mol}}^2)$ where k_{B} is the Boltzmann's constant, T is the temperature, P_0 is the pressure in the air rim and l_{mol} is the molecular diameter[41]. At a fixed temperature, the mean free path ratio between the pressure in the air rim chamber and that of the ambient is assumed to be $l/l_{\mathrm{atm}} = P_{\mathrm{atm}}/P_0$ where l_{atm} is the mean free path and P_{atm} is the pressure under ambient conditions. Thus, the Knudsen number can be written as[41]

$$\mathrm{Kn} = \frac{l}{L} = \frac{l_{\mathrm{atm}}}{L}\frac{P_{\mathrm{atm}}}{P_0}. \tag{2}$$

For the gas flow near $h_{\min}$, Kn ~ O(10^0) and therefore the slip effects at the wetting front are significant in our study.

Under the condition that the droplet and lubricating oil film are impermeable and cause gas flow upon impact, we predict the gas pressure to be given by the following dimensionless lubrication approximation accounting for the slip effects on both the droplet and the oil film[41]

$$\frac{\partial \overline{P}_{\mathrm{g}}}{\partial \overline{x}} = \overline{\mu}\frac{\partial^2 \overline{V}}{\partial \overline{z}^2}\bigg|_{z=h} = -\frac{6\overline{\mu}\left[1+2\mathrm{Kn}/\overline{h}+\overline{V}(2\mathrm{Kn}/\overline{h}+1)\right]}{\overline{h}^2\left[1+4\mathrm{Kn}/\overline{h}+12(\mathrm{Kn}/\overline{h})^2\right]}. \tag{3}$$

Here, the viscosity is normalized by $\overline{\mu} = \mu_{\mathrm{g}}/\mu_{\mathrm{l}}$, the height $\overline{h} = h_{\min}/L$, the velocity $\overline{V} = V/V_0$, and $\overline{x} = \overline{w} = w/L$ where a bar over the variable signifies a dimensionless parameter. We note that the wetting front is approximated here by using Cartesian coordinates instead of the cylindrical coordinate system (Figure 5 b-c) following the argument that the length scale of the inflection

point $w \sim \mathrm{O}(10^{-6})\,\mathrm{m}$ is much smaller than the wetted radius $R \sim \mathrm{O}(10^{-3})\,\mathrm{m}$. Equation (3) is originally derived for coating flows[41] that a solid plate in plunged into a still liquid bath. However, the current problem is that a droplet impacts on a non-moving thin oil film, which is presumably a perfectly smooth surface. We believe that the lubrication theory accounting for slip effects is relevant to both studies since the equation is derived for narrow gaps with a relative velocity between the surface and the wetting front. Equation 3 is then reduced to the following equation taking into account Maxwell slip on the gaseous phase,

$$\left|\frac{\partial \overline{P}_{\mathrm{g}}}{\partial \overline{x}}\right| = \frac{\overline{\mu}\left(1+\overline{V}\right)}{\overline{h}\left(\mathrm{Kn}+\overline{h}/6\right)}. \tag{4}$$

Given that slip effects are important, using an order of the magnitude argument (e.g., $\overline{V} \sim \mathrm{O}(1)$), the scaling for the gas pressure possibly forms in the dimensionless group,

$$\overline{P}_{\mathrm{g}} \sim \frac{\overline{\mu}\overline{V}\overline{w}}{\overline{h}\,\mathrm{Kn}}, \tag{5}$$

where the inertial effects in the drop are sufficiently small. The capillary pressure in the liquid phase is then made dimensionless by $\overline{P}_{\mathrm{l}} = P_{\sigma}/P$ where $P_{\sigma} \sim \sigma_{\mathrm{l}}/\kappa$ is the capillary pressure normalized by the pressure scale $P = \mu_{\mathrm{l}} V_0 / L$. The dimensionless capillary pressure can be scaled as

$$\overline{P}_{\mathrm{l}} \sim \sigma_{\mathrm{l}} \kappa \frac{L}{\mu_{\mathrm{l}} V_0}. \tag{6}$$

Now applying the air rim formation condition, $\overline{P}_{\mathrm{g}} \sim \overline{P}_{\mathrm{l}}$, we obtain that the critical capillary number, $\mathrm{Ca}_{\mathrm{c}} = \mu_{\mathrm{l}} V_{\mathrm{c}} / \sigma_{\mathrm{l}}$, where V_{c} is the critical contact line velocity at which the air rim forms – estimated by the initial contact line velocity V_0. The Ca_{c} will then inversely scale as the ambient pressure and we thus obtain the following scaling by balancing Eqns. (5) and (6),

$$\mathrm{Ca_c} \sim \frac{\bar{h}}{\bar{w}^2}\frac{P_{\mathrm{atm}}}{P_0}. \tag{7}$$

Varying the ambient pressure, droplet viscosity, surface tension and interfacial velocity (Table 1), 55 experiments are shown in Figure 6 where the dashed line depicts the inverse relationship between the Ca and normalized chamber pressure, P_0 / P_{atm} with a prefactor of 0.2. It should be noted that Sprittles[41] also numerically found the critical Ca to decrease with an increase in the chamber pressure but here we successfully provide the experimental evidence of $\mathrm{Ca_c} \sim P_{\mathrm{atm}} / P_0$. Figure 6 also implies that the ratio $\bar{h}/\bar{w}^2$ is a weak function of the chamber pressure for the conditions considered since the critical capillary number scales inversely with the chamber pressure. Under ambient conditions, the results show that below Ca ≈ 0.2, the instability is suppressed because the lubrication pressure in the air film cannot overcome the capillary pressure of the droplet. Above Ca ≈ 0.2, the air rim forms and the interfacial instability propagates due to the higher gas pressure relative to the capillary pressure in the vicinity of the contact line of the droplet. Below the ambient pressure, the transition from a stable contact line to an unstable contact line is observed at higher Ca which implies that, for the same droplet, a higher contact line velocity destabilizes the interface.

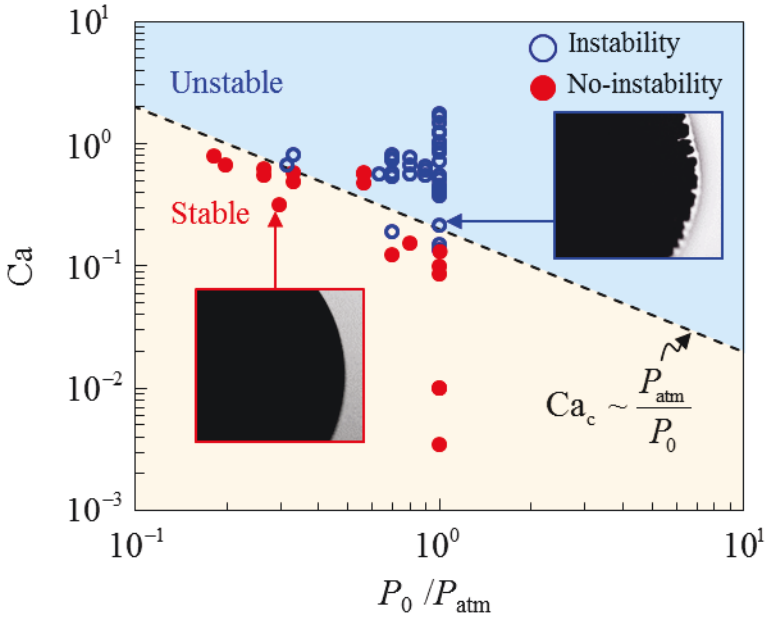

Figure 6. A scaling law plot depicting the formation or suppression of the fingering instability for capillary number versus normalized chamber pressure. The dashed line represents the inverse relationship between the critical capillary number and the chamber pressure, $\mathrm{Ca_c} \sim P_{atm} / P_0$. The insets are representative snapshots of the bottom view of TIRM images for the instability suppression (red dot) and propagation (blue circle).

Conclusion

Droplet impingement on perfectly smooth surfaces are rich with phenomenological anomalies such as the instability that has been observed on thin oil films for relatively low We ~ 10. In this study, we have systematically studied how well below the splash regime, there exists an interfacial instability that is caused by the buildup of the gas pressure near the contact line. We showed that this instability by directly measuring the growth of an air rim – which may only form when $P_g \sim P_l$ – demonstrating it to be a prerequisite to the contact line instability. The experimental results showed that the droplet velocity, viscosity and surface tension as well as the chamber pressure changes were shown to either help propagate the instability above a critical $\mathrm{Ca_c}$ or suppress it

where the $\mathrm{Ca}_c \sim P_{\mathrm{atm}} / P_0$. The results of this study are pertinent to the interfacial phenomenon under drop impact scenarios for a variety of industrial applications such as inkjet printing, coating technologies and liquid infused surfaces where interfacial instabilities are not favorable due to the entrainment of air disrupting smooth deposition or contact dynamics.

Acknowledgements

Support for this work was provided by the National Science Foundation under grant No. CMMI-1401438 and CBET-1705745. We thank Professor Howard A. Stone at Princeton University and Professor Vladimir Ajaev at Southern Methodist University for fruitful discussions. We also thank Charles Andersen for his help in image processing as well as Dong-Ook Kim and Ji-Hyun Ryu for experimental support.

References

1. Rein, M. Phenomena of liquid drop impact on solid and liquid surfaces. *Fluid Dynamics Research* **1993,** *12* (2), 61.

2. Yarin, A. L. Drop impact dynamics: Splashing, spreading, receding, bouncing. *Annual Review of Fluid Mechanics* **2006,** *38* (1), 159-192.

3. Josserand, C.; Thoroddsen, S. T. Drop impact on a solid surface. *Annual Review of Fluid Mechanics* **2016,** *48* (1), 365-391.

4. Joung, Y. S.; Buie, C. R. Aerosol generation by raindrop impact on soil. *Nature Communications* **2015,** *6*, 6083.

5. Lafuma, A.; Quéré, D. Slippery pre-suffused surfaces. *Europhysics Letters* **2011,** *96* (5), 56001.

6. Wong, T.-S.; Kang, S. H.; Tang, S. K. Y.; Smythe, E. J.; Hatton, B. D.; Grinthal, A.; Aizenberg, J. Bioinspired self-repairing slippery surfaces with pressure-stable omniphobicity. *Nature* **2011,** *477* (7365), 443-447.

7. Subramanyam, S. B.; Rykaczewski, K.; Varanasi, K. K. Ice adhesion on lubricant-impregnated textured surfaces. *Langmuir* **2013,** *29* (44), 13414-13418.

8. Pack, M.; Hu, H.; Kim, D.-O.; Yang, X.; Sun, Y. Colloidal drop deposition on porous substrates: competition among particle motion, evaporation, and infiltration. *Langmuir* **2015,** *31* (29), 7953-7961.

9. Panão, M. R. O.; Moreira, A. L. N. Experimental study of the flow regimes resulting from the impact of an intermittent gasoline spray. *Experiments in Fluids* **2004,** *37* (6), 834-855.

10. Aziz, S. D.; Chandra, S. Impact, recoil and splashing of molten metal droplets. *International Journal of Heat and Mass Transfer* **2000,** *43* (16), 2841-2857.

11. Kalantari, D.; Tropea, C. Spray impact onto flat and rigid walls: Empirical characterization and modelling. *International Journal of Multiphase Flow* **2007,** *33* (5), 525-544.

12. Mudawar, I.; Estes, K. A. Optimizing and predicting CHF in spray cooling of a square surface. *Journal of Heat Transfer* **1996,** *118* (3), 672-679.

13. Dorr, G. J.; Wang, S.; Mayo, L. C.; McCue, S. W.; Forster, W. A.; Hanan, J.; He, X. Impaction of spray droplets on leaves: influence of formulation and leaf character on shatter, bounce and adhesion. *Experiments in Fluids* **2015,** *56* (7), 143.

14. Fitt, B. D.; McCartney, H.; Walklate, P. The role of rain in dispersal of pathogen inoculum. *Annual Review of Phytopathology* **1989,** *27* (1), 241-270.

15. Gilet, T.; Bourouiba, L. Rain-induced ejection of pathogens from leaves: revisiting the hypothesis of splash-on-film using high-speed visualization. The Society for Integrative and Comparative Biology, 2014.

16. Gilet, T.; Bourouiba, L. Fluid fragmentation shapes rain-induced foliar disease transmission. *Journal of The Royal Society Interface* **2015,** *12* (104), 20141092.

17. Smith, H.; Levy, G.; Shainberg, I. Water-droplet energy and soil amendments: Effect on infiltration and erosion. *Soil Science Society of America Journal* **1990,** *54* (4), 1084-1087.

18. Kolinski, J.; Mahadevan, L.; Rubinstein, S. Drops can bounce from perfectly hydrophilic surfaces. *Europhysics Letters* **2014,** *108* (2), 24001.

19. Xu, L.; Zhang, W. W.; Nagel, S. R. Drop splashing on a dry smooth surface. *Physical Review Letters* **2005,** *94* (18), 184505.

20. Kolinski, J. M.; Rubinstein, S. M.; Mandre, S.; Brenner, M. P.; Weitz, D. A.; Mahadevan, L. Skating on a film of air: drops impacting on a surface. *Physical review letters* **2012,** *108* (7), 074503.

21. Bouwhuis, W.; van der Veen, R. C. A.; Tran, T.; Keij, D. L.; Winkels, K. G.; Peters, I. R.; van der Meer, D.; Sun, C.; Snoeijer, J. H.; Lohse, D. Maximal air bubble entrainment at liquid-drop impact. *Physical Review Letters* **2012,** *109* (26), 264501.

22. de Ruiter, J.; Oh, J. M.; van den Ende, D.; Mugele, F. Dynamics of collapse of air films in drop impact. *Physical Review Letters* **2012,** *108* (7), 074505.

23. Latka, A. Thin-sheet creation and threshold pressures in drop splashing. *Soft matter* **2017,** *13* (4), 740-747.

24. Pack, M.; Hu, H.; Kim, D.; Zheng, Z.; Stone, H. A.; Sun, Y. Failure mechanisms of air entrainment in drop impact on lubricated surfaces. *Soft Matter* **2017,** *13* (12), 2402-2409.

25. Mandre, S.; Mani, M.; Brenner, M. P. Precursors to splashing of liquid droplets on a solid surface. *Physical review letters* **2009,** *102* (13), 134502.

26. Rein, M.; Delplanque, J.-P. The role of air entrainment on the outcome of drop impact on a solid surface. *Acta mechanica* **2008,** *201* (1), 105-118.

27. Thoroddsen, S. T.; Thoraval, M.-J.; Takehara, K.; Etoh, T. Micro-bubble morphologies following drop impacts onto a pool surface. *Journal of Fluid Mechanics* **2012,** *708*, 469-479.

28. Thoraval, M.-J.; Takehara, K.; Etoh, T.; Thoroddsen, S. T. Drop impact entrapment of bubble rings. *Journal of Fluid Mechanics* **2013,** *724*, 234-258.

29. Driscoll, M. M.; Stevens, C. S.; Nagel, S. R. Thin film formation during splashing of viscous liquids. *Physical Review E* **2010,** *82* (3), 036302.

30. Thoroddsen, S. T.; Takehara, K.; Etoh, T. Bubble entrapment through topological change. *Physics of Fluids* **2010,** *22* (5), 051701.

31. Li, E.; Vakarelski, I. U.; Thoroddsen, S. T. Probing the nanoscale: the first contact of an impacting drop. *Journal of Fluid Mechanics* **2015,** *785*.

32. Allen, R. F. The role of surface tension in splashing. *Journal of Colloid and Interface Science* **1975,** *51* (2), 350-351.

33. Lee, C.; Kim, H.; Nam, Y. Drop impact dynamics on oil-infused nanostructured surfaces. *Langmuir* **2014,** *30* (28), 8400-8407.

34. Thoroddsen, S.; Sakakibara, J. Evolution of the fingering pattern of an impacting drop. *Physics of fluids* **1998,** *10* (6), 1359-1374.

35. Xu, L. Liquid drop splashing on smooth, rough, and textured surfaces. *Physical Review E* **2007,** *75* (5), 056316.

36. Liu, Y.; Tan, P.; Xu, L. Kelvin–Helmholtz instability in an ultrathin air film causes drop splashing on smooth surfaces. *Proceedings of the National Academy of Sciences* **2015,** *112* (11), 3280-3284.

37. Weinstein, S. J.; Ruschak, K. J. Coating flows. *Annu. Rev. Fluid Mech.* **2004,** *36*, 29-53.

38. Kistler, S. Hydrodynamics of wetting. *Wettability* **1993,** *6*, 311-430.

39. Vandre, E.; Carvalho, M.; Kumar, S. On the mechanism of wetting failure during fluid displacement along a moving substrate. *Physics of Fluids* **2013,** *25* (10), 102103.

40. Sprittles, J. E. Kinetic effects in dynamic wetting. *Physical Review Letters* **2017,** *118* (11), 114502.

41. Sprittles, J. E. Air entrainment in dynamic wetting: Knudsen effects and the influence of ambient air pressure. *Journal of Fluid Mechanics* **2015,** *769*, 444-481.

42. Liu, C.-Y.; Vandre, E.; Carvalho, M. S.; Kumar, S. Dynamic wetting failure and hydrodynamic assist in curtain coating. *Journal of Fluid Mechanics* **2016,** *808*, 290-315.

43. Marchand, A.; Chan, T. S.; Snoeijer, J. H.; Andreotti, B. Air entrainment by contact lines of a solid plate plunged into a viscous fluid. *Physical Review Letters* **2012,** *108* (20), 204501.

44. Li, E. Q.; Langley, K. R.; Tian, Y. S.; Hicks, P. D.; Thoroddsen, S. T. Double Contact During Drop Impact on a Solid Under Reduced Air Pressure. *Physical review letters* **2017,** *119* (21), 214502.

45. Hecht, E. *Optics*; Pearson Education2015.

46. Shirota, M.; van Limbeek, M. A. J.; Lohse, D.; Sun, C. Measuring thin films using quantitative frustrated total internal reflection (FTIR). *The European Physical Journal E* **2017,** *40* (5), 54.

47. Kolinski, J. M.; Mahadevan, L.; Rubinstein, S. M. Lift-off instability during the impact of a drop on a solid surface. *Physical Review Letters* **2014,** *112* (13), 134501.

48. Rivière, D.; Leroy, C.; Guyon, E.; Hulin, J. P. An optical study of thin interfacial liquid films using total reflection of light. *Experiments in Fluids* **1987,** *5* (5), 349-354.

49. Howland, C. J.; Antkowiak, A.; Castrejón-Pita, J. R.; Howison, S. D.; Oliver, J. M.; Style, R. W.; Castrejón-Pita, A. A. It's Harder to Splash on Soft Solids. *Physical review letters* **2016,** *117* (18), 184502.

50. Shirota, M.; van Limbeek, M. A.; Sun, C.; Prosperetti, A.; Lohse, D. Dynamic leidenfrost effect: Relevant time and length scales. *Physical Review Letters* **2016,** *116* (6), 064501.

51. Klaseboer, E.; Manica, R.; Chan, D. Y. C. Universal behavior of the initial stage of drop impact. *Physical Review Letters* **2014,** *113* (19), 194501.

52. Lee, J. S.; Weon, B. M.; Je, J. H.; Fezzaa, K. How does an air film evolve into a bubble during drop impact? *Physical Review Letters* **2012,** *109* (20), 204501.

53. van Dam, D. B.; Le Clerc, C. Experimental study of the impact of an ink-jet printed droplet on a solid substrate. *Physics of Fluids* **2004,** *16* (9), 3403-3414.

54. Thoroddsen, S.; Etoh, T.; Takehara, K.; Ootsuka, N. The air bubble entrapped under a drop imacting on a solid surface. *Journal of Fluid Mechanics* **2005,** *545*, 203-212.

55. Blake, T. D. The physics of moving wetting lines. *Journal of colloid and interface science* **2006,** *299* (1), 1-13.

Table of Contents Graphic